

Time Variability of Surface-Layer Characteristics over a Mountain Ridge in the Central Himalayas During the Spring Season

Raman Solanki^{1,2} · Narendra Singh¹  ·
N. V. P. Kiran Kumar³ · K. Rajeev³ · S. K. Dhaka⁴

Received: 22 January 2015 / Accepted: 13 October 2015 / Published online: 28 October 2015
© Springer Science+Business Media Dordrecht 2015

Abstract We present the diurnal variations of surface-layer characteristics during spring (March–May 2013) observed near a mountain ridge at Nainital (29.4°N, 79.5°E, 1926 m above mean sea level), a hill station located in the southern part of the central Himalayas. During spring, this region generally witnesses fair-weather conditions and significant solar heating of the surface, providing favourable conditions for the systematic diurnal evolution of the atmospheric boundary layer. We mainly utilize the three-dimensional wind components and virtual temperature observed with sonic anemometers (sampling at 25 Hz) mounted at 12- and 27-m heights on a meteorological tower. Tilt corrections using the planar-fit method have been applied to convert the measurements to streamline-following coordinate system before estimating turbulence parameters. The airflow at this ridge site is quite different from slope flows. Notwithstanding the prevalence of strong large-scale north-westerly winds, the diurnal variation of the mountain circulation is clearly discernible with the increase of wind speed and a small but distinct change in wind direction during the afternoon period. Such an effect further modulates the surface-layer water vapour content, which increases during the daytime and results in the development of boundary-layer clouds in the evening. The sensible heat flux (H) shows peak values around noon, with its magnitude increasing from March ($222 \pm 46 \text{ W m}^{-2}$) to May ($353 \pm 147 \text{ W m}^{-2}$). The diurnal variation of turbulent kinetic energy (e) is insignificant during March while its mean value is enhanced by 30–50% of the post-midnight value during the afternoon (1400–1600 IST), delayed by ≈ 2 h compared to the peak in H . This difference between the phase variations of incoming shortwave flux, H and e primarily arise due to the competing effects of turbulent eddies produced by thermals and wind shear, the latter increase significantly with time until nighttime during April–May. Variations of the standard deviations of vertical wind normalized with friction velocity (σ_w/u_*) and

✉ Narendra Singh
narendra@aries.res.in

¹ Aryabhata Research Institute of Observational Sciences, Nainital, India

² Department of Physics and Astrophysics, University of Delhi, Delhi, India

³ Space Physics Laboratory, Vikram Sarabhai Space Centre, Trivandrum, India

⁴ Radio and Atmospheric Physics Lab., Rajdhani College, University of Delhi, New Delhi, India

temperature normalized with scaling temperature (σ_θ/T_*) as functions of stability parameter (z/L) indicate that they follow a power-law variation during unstable conditions, with an index of $1/3$ for the former and $-1/3$ for the latter. The coefficients defining the above variations are found in agreement with those derived over flat as well as complex terrain.

Keywords Atmospheric surface layer · Micrometeorology · Momentum flux · Mountains · Sensible heat flux · Turbulence · Wind shear

1 Introduction

Over homogeneous flat surfaces, the diurnal evolution of the atmospheric boundary layer (ABL) is primarily controlled by the variations in the net radiation balance, energy fluxes, surface characteristics (including vegetation and soil moisture), and the background meteorological conditions (Stull 1988). In contrast, the diurnal evolution of ABL meteorological parameters, energy and momentum fluxes and circulation over mountainous region are further substantially modulated by topography and the associated land-cover heterogeneities (Whiteman 1990; Moraes et al. 2005; Vickers and Mahrt 2006b; Rotach and Zardi 2007; Bianco et al. 2011). Strength of the large-scale prevailing flow and its orientation with the orography, as well as the sheltering effects produced by the mountain and trees, further add to the complexities in the evolution of the ABL over mountainous terrain (e.g., Mahrt 2006; Helgason and Pomeroy 2012). Knowledge of the diurnal variations of meteorological parameters and surface-layer characteristics is essential for improving the understanding of mountain meteorology, assessment of the impact of topography in regulating ABL processes, as well as the accurate parametrization of the ABL, in order to improve the performance of atmospheric circulation models (e.g., Helgason and Pomeroy 2012). Though, the knowledge of the basic circulation features over mountain terrain has been reasonably established (e.g., Whiteman 2000), the measurements and in-depth understanding of ABL characteristics over such terrain are rather poor as compared to flat homogeneous surfaces (e.g., Moraes et al. 2005; Nadeau et al. 2013). This is primarily because accurate observations of surface-layer characteristics over mountainous terrain are difficult to make (e.g., Wilczak et al. 2001; Yuan et al. 2011), as these observations require a sufficiently large uniform fetch, especially in the upwind direction (Stull 1988; Arya 2001; Moraes et al. 2005; Rotach and Zardi 2007).

Diurnal temperature variations on inclined surfaces produce lateral density gradients that drive the katabatic and anabatic winds along with the drainage circulation, development of which strongly depends upon the topography, surface type, background winds, and the characteristics of boundary-layer turbulence (Barr and Orgill 1989; Li and Atkinson 1999; Papadopoulos and Helmis 1999; Hughes et al. 2007). Higher air temperatures over steeper slopes result in stronger drainage flows and greater downward mixing of heat towards the surface (Mahrt and Heald 1983). In general, downslope flows persist for less than an hour after sunrise, and strong regional circulations (either as part of synoptic or mesoscale circulations) might hamper this normal development of a local slope circulation and strong nocturnal surface inversion (Whiteman 2000; Stewart et al. 2002). However, over mountainous terrain, the above mentioned local circulations may be more dominant near the surface, while the effect of regional circulations may be significant at higher levels (Mahrt et al. 2001).

The accuracy of atmospheric circulation and dispersion models significantly depends upon the parametrization of turbulence and energy exchanges. Diurnal variations in the surface-layer characteristics and mountain circulations play a vital role in regulating the transport or trapping of pollutants from valleys (Kleissl et al. 2007) and is a decisive factor in the

occurrence of atmospheric pollution episodes in the Himalayan region (Ramanathan and Ramana 2005; Pant et al. 2006; Panday and Prinn 2009; Solanki et al. 2013). Unlike flat terrain, characteristics of the surface-layer and turbulence parameters over complex terrain are not well understood (e.g., Moraes et al. 2005). Though the results obtained from several experimental studies carried out over complex terrain show general agreement, they also show major differences and hence additional data in data-sparse mountainous terrain are essential for improved understanding of surface-layer and ABL characteristics (e.g., Moraes et al. 2005; Martins et al. 2009; Katurji et al. 2011). The present observations are relevant in this context, however, a few studies on the ABL circulation over the northern Himalayas have been carried out in the past (Sun et al. 2007; Chen et al. 2013). Observations of surface-layer characteristics and their diurnal evolution are non-existent in the southern Himalayas; therefore, such observations would be of paramount importance in quantifying the mountain circulation feature and providing insight into the transport of aerosol and trace species to the Himalayas from the adjoining plains.

The mean streamlines near the surface in a sloping terrain are expected to be parallel to the terrain, unless flow separation occurs. Over sloping terrain, the estimation of surface-layer turbulence and fluxes requires a mean streamline-following coordinate system. Generally, sonic anemometers are placed with the z -axis oriented perpendicular to the local surface to avoid artefacts in the measured vertical winds caused by the interaction of horizontal winds with the terrain. For anemometers placed in the true vertical coordinate system (z -axis along the direction of gravity) in a sloping terrain, fluctuations in the streamwise velocity component creates an apparent stress, the magnitude of which varies with slope angle relative to wind direction (Geissbuhler et al. 2000; Wilczak et al. 2001; Yuan et al. 2007, 2011; Richiardone et al. 2008). In the present study, the tilt corrections are applied to sonic anemometer data using the planar-fit method (PFM; Wilczak et al. 2001; Yuan et al. 2007, 2011; Richiardone et al. 2008), thus making the measurements comparable to those over other sites. In principle, the scaling methods for turbulence variables observed over flat horizontally homogenous terrain are not applicable as such in complex terrain because of the slope winds. However, studies on the flow and exchange characteristics within and above steep vegetated terrain have shown that many statistical properties typical of flat terrain are also observed in complex terrain (Rotach and Zardi 2007). The variations of the standard deviation of vertical wind normalized with friction velocity and the standard deviation of temperature normalized with scaling temperature are used here to assess the quality of data and turbulence parameters derived for non-ideal conditions such as complex terrain (Foken and Wichura 1996; Geissbuhler et al. 2000).

The main objective of the study is to investigate the diurnal variations of micrometeorological parameters, surface-layer fluxes of energy and momentum, and turbulence characteristics over the south-central Himalayan region during the spring season. The results presented are also useful for understanding the temporal variations of aerosols and trace gases and their transport over the sub-Himalayan region. Indian standard time (IST = UTC + 5:30 h) is used throughout.

2 Experimental Site and Instrumentation

The observational site is situated at the Aryabhata Research Institute of Observational Sciences (ARIES) campus at Manora Peak, Nainital (29.4°N, 79.5°E, altitude 1926 m above mean sea level), a high altitude station in the southern part of the central Himalayas (Fig. 1a), established under the Network of Observatories for Boundary Layer Experiment (NOBLE)

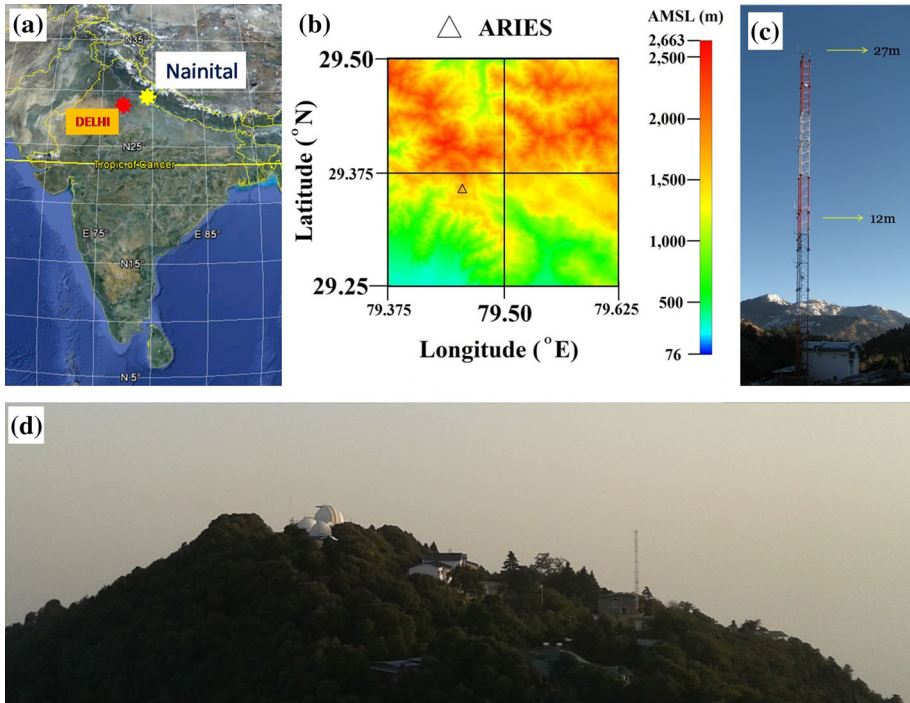


Fig. 1 **a** Geographical location of Nainital, **b** topography image of the region around the ARIES, Nainital site, **c** self supported meteorological tower with instruments mounted at 12- and 27-m levels, and **d** photograph of the site taken from the nearby peak of almost equal elevation as Manora Peak, situated in the north-east direction

project of Indian Space Research Organization's Geosphere–Biosphere Program (ISRO-GBP). The region encompasses a series of ridges and valleys. On a wider perspective, elevation of the Himalayan mountain range in the Indian region generally increases northward; within a distance of 120 km around Nainital, the surface elevation increases northward from <300 m (in the northern part of the Gangetic plain) to above 5000 m in the north. On the local scale (which is important in affecting surface-layer characteristics), the site is located close to a mountain ridge (Fig. 1b). The ridge axis is aligned approximately along the north-west direction. Location of the meteorological tower with respect to the local ridge is shown in Fig. 1d. The 27-m meteorological tower is installed on the western side of the peak at an altitude ≈ 15 m lower than the mountain peak (base of the tower), and at a horizontal separation of ≈ 150 m between the two. The slope within a horizontal distance of 1 km is about 16° on the western side of the mountain crest (where the observation site is located), while on a relatively larger scale (horizontal distance of 10–15 km), the slope ranges from 4° to 8° on all sides; the slope towards the north is rather small within this horizontal distance. The north-western valley adjoining the ridge is covered with trees, up to a horizontal distance of over 400 m, which is primarily the upwind direction during the spring season. However, the area near the tower and the mountain top is rather barren.

The 27-m meteorological tower is instrumented at two levels: 12 and 27 m (Fig. 1c). Booms of 2-m length are provided for mounting the sensors, which comprise a three-axis sonic anemometer (make METEK, GmBH, Germany, model “USA-1 Scientific”), slow response

hygristor and air temperature sensors (PT-100 1/3 DIN, 4 wire-technique). All sensors have been factory calibrated before mounting on the tower. The three orthogonal components of wind and acoustic temperature are measured using the sonic anemometers operating at 25 Hz. Sonic anemometer USA-1 is equipped with a three-dimensional (3D) head-correction for an angle of attack in the range of $\pm 45^\circ$. The correction factors incorporated in the sensor are determined using wind-tunnel tests carried out and implemented by the manufacturer. This function corrects the flow distortion of the sensor head based on the horizontal and the vertical wind components. The acoustic temperature (T_s) measured using the sonic anemometer is converted to virtual temperature (T_v) using the equation $T_s \approx T_v - 0.02p$ (p being the partial pressure due to water vapour). As the observations used were carried out very near a mountain ridge, with the top level sonic anemometer located above the ridge surface level, the sonic anemometers were mounted in a true vertical position (in the direction of gravity), rather than along the local normal (perpendicular to the local surface). Tilt correction has been applied to these measurements before estimating the turbulence parameters and fluxes. The humidity and temperature measured using the slow response sensors are averaged for 1 min, while surface meteorological observations and the incoming shortwave radiative flux are observed using a collocated automatic weather station installed by the Indian Meteorological Department. These instruments are mounted at 10-m height above ground level at the mountain top (which is about 150 m from the sonic anemometer tower horizontally) and mounted vertically, as the observations are taken at mountain top. Hourly-averaged meteorological data are utilized for background meteorological conditions over the site, together with local weather conditions (sky condition, amount and type of clouds, appearance of fog, convection, and thunderstorms in the vicinity of the experimental site), noted manually every 3 h.

3 Data Processing and Methodology

We focus on the diurnal evolution of surface-layer characteristics during fair-weather events, and hence days having large-scale cloudiness or convection (assessed on the basis of temporal variations in incoming shortwave flux and weather events recorded in the log book) are avoided. However, formation of boundary-layer clouds (as part of the ABL evolution) is a regular feature during most of the days in spring, and such days are included in the study. During March–May 2013, 46 mostly cloud-free days (except for the ABL clouds) are selected, discarding days with significant cloudiness or precipitation. In tandem with the daytime surface heating and thermal instability of the surface layer, the turbulent kinetic energy (e) as well as the associated vertical fluxes of momentum and heat are expected to undergo systematic diurnal variations. The turbulence intensity is quantified through the magnitudes of e , whereas the exchange of energy and momentum fluxes are quantified through sensible heat flux (H) and vertical momentum flux (τ), respectively.

Since the measurements were made over sloping terrain, the data have been corrected for sensor tilt (with respect to local normal) by converting to a streamline-following coordinate system. Studies reported in the literature show that the planar-fit technique has considerable advantages in sonic anemometer tilt correction, compared to the double and triple-rotation methods for rotation of the anemometer with respect to streamlines (Wilczak et al. 2001; Yuan et al. 2007). Wilczak et al. (2001) compared different methods for correcting tilt angles relative to the mean streamline coordinate system, and showed that the double and triple rotation methods might lead to significant run-to-run stress errors due to sampling errors of the mean vertical wind velocity and cross-wind stress. The PFM has been shown to reduce

the run-to-run stress errors and provide unbiased estimates of lateral stress (Wilczak et al. 2001). The PFM estimates a set of tilt angles for a set of data runs and is less susceptible to sampling errors. One of the conditions for the application of PFM is that the tilt of the sonic anemometer and its orientation with respect to the terrain slope should not be altered over the duration of the data being analyzed, from which the tilt angles are estimated (Wilczak et al. 2001). As the PFM provides an offset of the mean vertical wind speed, it can also be used to estimate the vertical advection (e.g., that caused by a mountain valley circulation) using the residual vertical winds obtained after the PFM rotation (e.g., Yuan et al. 2007). In this study, the data obtained from the sonic anemometers mounted in true vertical direction near the mountain ridge are converted to the streamline-following coordinate system using the PFM algorithm in Wilczak et al. (2001) and Yuan et al. (2007, 2011). While Wilczak et al. (2001) derived a single set of tilt angles for all wind directions; Yuan et al. (2007, 2011) suggested that the tilt angles for different mean wind directions (typically estimated at 30° intervals in wind direction) could be different. However, during most of the observation period reported here, the winds are predominantly in the north-westerly direction (270–310°), and the dataset for other wind directions were rather small to reliably estimate the tilt angle corrections at different wind directions. Hence, herein, the mean tilt angles are estimated by considering the whole set of data for the spring season. Observations for a total of 46 days have been used for estimating the mean tilt angles using the PFM. Values of the regression coefficients b_0 , b_1 and b_2 (Eq. 4 of Yuan et al. 2007) obtained are -0.0059 , 0.2211 , and -0.2872 , respectively, and the estimated tilt angles are -12.0° (angle α in the x - z plane) and -16.0° (angle β in the y - z plane).

The fluctuations in the three orthogonal wind components (u , v , and w) and virtual temperature measured using the sonic anemometers, after applying the PFM for tilt correction, are utilized for estimating e , τ and H using the eddy-correlation method (Kaimal and Finnigan 1994; Aubinet et al. 2012). The quantities e , H and τ are computed from,

$$e = \frac{1}{2} (\overline{u'^2} + \overline{v'^2} + \overline{w'^2}), \tag{1}$$

$$H = \rho C_p (\overline{w'\theta'_v}), \tag{2}$$

$$\tau = \rho \sqrt{(\overline{u'w'})^2 + (\overline{v'w'})^2}, \tag{3}$$

where u' , v' , w' and θ'_v are the turbulent fluctuations in the orthogonal wind components and virtual potential temperature, respectively. These fluctuations at 27-m height are estimated and averaged for a period of 30 min; the overbar represents an average over 30-min duration, and where ρ and C_p represent atmospheric density and the isobaric specific heat of air, respectively.

The stability of the surface layer is characterized through the dimensionless length scale z/L , where z is the height of observation (here 12 and 27 m) and L is the Obukhov length, $L = -u_*^3 / (k \frac{g}{\theta_v} \overline{w'\theta'_v})$, and the friction velocity (u_*) and scaling temperature (T_*) are given by $u_* = \sqrt{\tau/\rho}$, $T_* = -\frac{\overline{w'\theta'_v}}{u_*}$.

In the above κ is the von Karman constant (=0.4), and g is the acceleration due to gravity. Mean winds, temperature, energy and momentum fluxes, stability parameter, and normalized standard deviations of velocity and temperature fluctuations are estimated for each 30-min time bins during the observation period. Monthly mean diurnal variations of the above parameters are obtained by averaging the respective values for the same time bins. Variations of

different parameters with stability are obtained by averaging the respective values at constant intervals of z/L .

4 Results

4.1 Background Meteorological Conditions

During spring season, the study region experiences generally fair-weather and large surface heating by the incoming solar radiation, which favour significant diurnal variations of surface-layer energetics, evolution of ABL and boundary-layer circulation. Space borne regional distribution of clouds shows that the 10° – 30° N latitude belt over the Indian region is almost cloud-free ($<20\%$ monthly mean cloudiness) during the spring season (Meenu et al. 2007, 2010). This is caused by the large-scale tropospheric subsidence associated with the descending limb of the Hadley cell which is located above this region during spring, favouring fair weather conditions and significant diurnal evolution of ABL. In contrast, large-scale cloudiness and precipitation occur over this region during summer, suppressing the clear diurnal evolution of ABL. During winter, the site experiences snowfall on a few days as a result of western disturbances.

Figure 2 depicts a comparison of the seasonal mean synoptic circulation at 800-hPa level over the region during the four seasons, obtained from the European Centre for Medium-Range Weather Forecasts (ECMWF)-interim reanalysis data. Figure 2a indicates the large-scale advection of strong north-westerly winds over the Indo-Gangetic plain and the south-central Himalayas during the spring season. The seasonal mean wind (at 800-hPa level) in this belt ranges from 6 to 10 m s^{-1} ; the observational site (marked by the symbol 'o') is located at the northern fringe of this strong north-westerly wind regime during the spring season. In contrast, the mean winds associated with the regional circulation are weaker and significantly variable during the other seasons.

4.2 Diurnal Variations of Meteorological Parameters

Figure 3 shows the monthly mean diurnal variations of the incoming solar radiative flux (shortwave flux, $S\downarrow$) observed at the site during March, April, and May 2013. The vertical bars represent the respective standard deviations. The $S\downarrow$ values at noon attain a peak of 1000 – 1100 W m^{-2} over this hill station during spring season. Such high values are due to the favourable solar declination, high altitude of the station and clear sky conditions prevailing during this season. The $S\downarrow$ values during April and May are about 100 – 150 W m^{-2} more than the corresponding values during March, indicating an increase in surface heating during April–May. The standard deviation in $S\downarrow$ is an indicator of the presence of isolated cloud patches during each month. Larger standard deviations of $S\downarrow$ observed during the afternoon are due to the increase in the frequency of occurrence of boundary-layer clouds (visual observations) during the afternoon.

Contour maps of the diurnal and seasonal variations of horizontal wind speed and wind direction observed using the sonic anemometer at the 27-m level are given in Fig. 4. Corresponding contour map of the horizontal wind shear between 12- and 27-m levels are also shown in Fig. 4. The monthly mean diurnal variations of wind speed and wind direction at the 12- and 27-m levels during March, April and May are shown in Fig. 5. Figures 4 and 5 show that, throughout the spring season, the diurnal variation of wind speed is manifested by two prominent maxima and minima: the minima occur around pre-noon (0900–1100 IST) and

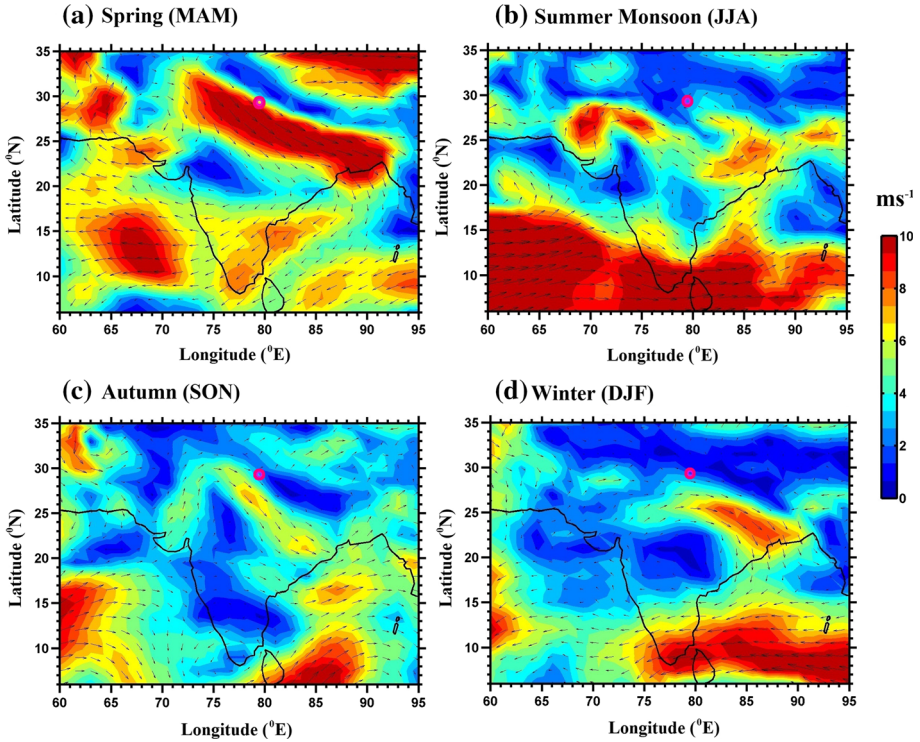


Fig. 2 Seasonal mean winds at 800-hPa level during **a** spring (March–May), **b** summer monsoon (June–August), **c** autumn (September–November), and **d** winter (December–February) seasons of 2013, obtained from the ECMWF-interim reanalysis data. The colour scale indicates wind speed

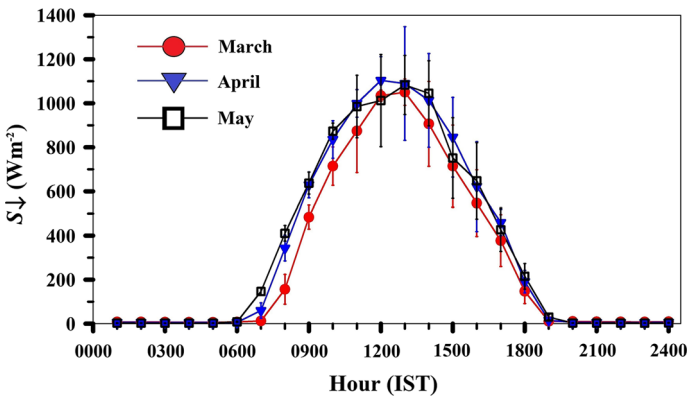
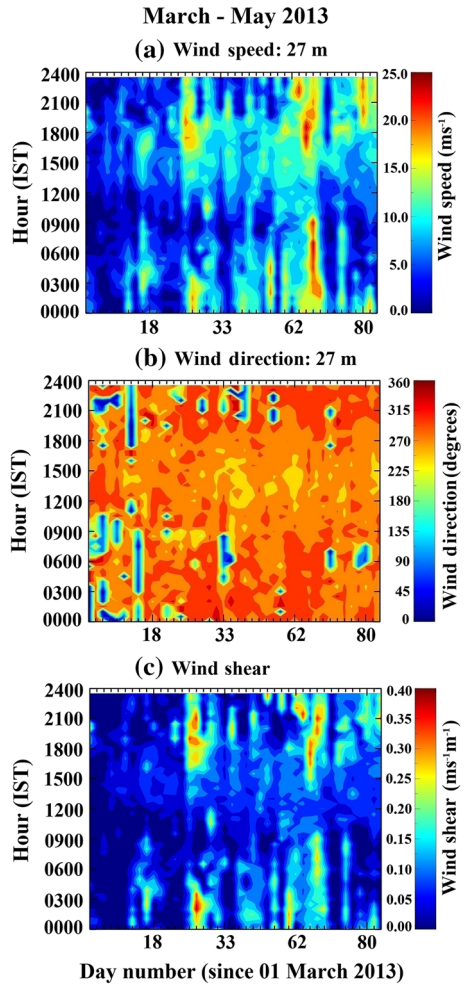


Fig. 3 Monthly mean diurnal variations of the incoming shortwave solar radiative flux (S_{\downarrow}) during March, April and May 2013 observed at the site. Vertical bars indicate the standard deviations

midnight (2300–0100 IST), while the maxima occur in the early morning (\approx 0400–0600 IST) and late-afternoon and evening (\approx 1500–1900 IST). Among them, the smallest and highest wind speeds generally occur around the pre-noon and evening periods, respectively. The average wind speed systemically increases with the advancement of the season. The wind

Fig. 4 Contour maps of the diurnal and seasonal variations of **a** horizontal wind speed, and **b** wind direction observed using sonic anemometer at 27-m level. **c** Same as **a** but for the horizontal wind shear between 12- and 27-m levels. The *x*-axis represents day number and the *y*-axis shows time of the day. The colour bars on the right side of each panel indicate their respective scales



direction is predominantly north-westerly; however, during the periods of minimum wind speed observed during the pre-noon and midnight period, the wind direction occasionally changes to easterly. The wind speed observed at 27 m is always larger than that at 12 m. At 27 m, the probability of occurrence of wind speeds $>7 \text{ m s}^{-1}$ is $\approx 34\%$ during the nighttime while it is only $\approx 22\%$ during the daytime. At the 12-m level, the above probability is 12% during the nighttime and rare ($<3\%$) during the daytime. The day–night difference in wind speed is largest at the 27-m level. During April and May, the nighttime peak wind speed observed at 27-m level sometimes exceeds 10 m s^{-1} . Such events are also associated with significant wind shear (exceeding $0.25 \text{ m s}^{-1} \text{ m}^{-1}$) between the 12- and 27-m levels, which has the potential for generating turbulent eddies and increasing the vertical mixing of surface-layer air. Phase of the diurnal variation of wind shear is same as that of wind speed, with both of them maximizing around 0400–0600 IST and 1500–1900 IST; the peak wind shear increases from March (typically $\approx 0.06 \text{ s}^{-1}$) to April–May (typically 0.2 s^{-1}).

As evident from Fig. 5, the wind directions at both the levels are remarkably similar during night, but show small and consistent differences during the daytime. This aspect

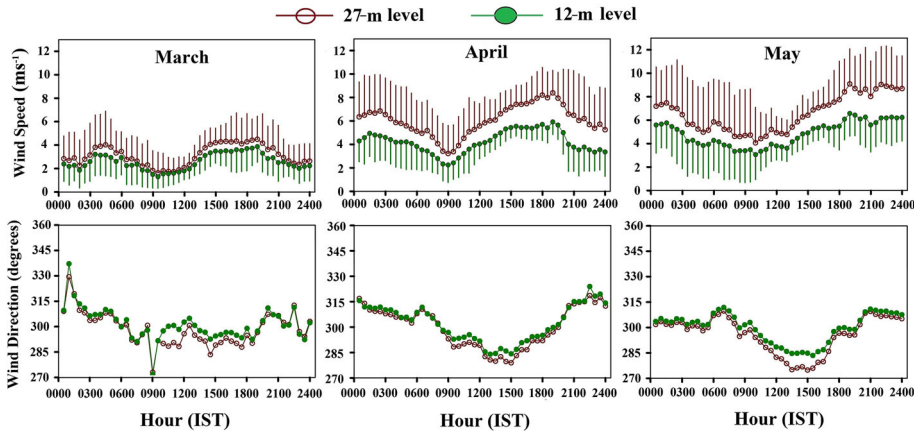


Fig. 5 Monthly mean diurnal variations of horizontal wind speed and wind direction at the 12- and 27-m levels during March (*left panel*), April (*middle panel*) and May 2013 (*right panel*)

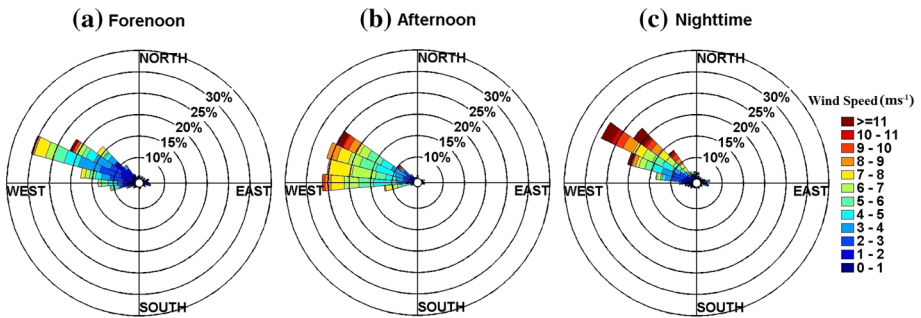


Fig. 6 Wind roses at the 27-m level for **a** forenoon (0700–1200 IST), **b** afternoon (1300–1800 IST) and **c** night (1900–0600 IST) during the spring season of 2013

is investigated further in Fig. 6, which shows wind roses during the forenoon: 0700–1200 IST; afternoon (1300–1800 IST) and night (1900–0600 IST). In general, the wind direction is predominantly west-north-westerly with rather narrow spread (wind direction is mostly within a cone of 285° and 305°) during the forenoon, while the spread in wind direction is rather wide (nearly equal probability for winds in the cone of 265°–305°) during the afternoon. During night, the wind is strong and mostly flows from a cone of 295° to 315°. Enhancement in the probability of occurrence of westerly winds during the afternoon period, similarity in the wind directions west-north-westerly during the night and forenoon periods, and the considerable enhancement in wind speed during the night are particularly notable. However, even during the afternoon period, the strongest winds (> 10 m s⁻¹) are generally north-westerly, rather than westerly.

The diurnal variations of relative humidity (*RH*) during March, April and May were also analyzed. In March, dry condition (mean *RH* < 40 %) prevails during the post-midnight and morning period and *RH* values generally increase during the daytime until about 1500–1600 IST, when the mean *RH* is > 80 % and sometimes reaches saturation level. The relative humidity undergoes a systematic decrease during the post-sunset period. Visual observations show the boundary-layer cloud formation during the afternoon period and their dissipation

after the sunset, especially in March. The evening enhancement of RH is smaller during April–May, while the post-midnight dry conditions prevail during this period as well. The diurnal variation of mixing ratio is most prominent in March when it increases from 4.1 g kg^{-1} at 0700 IST to 10.5 g kg^{-1} at 1600–1700 IST. In April, the monthly mean diurnal variation of mixing ratio shows an increase from 4.3 g kg^{-1} at 0600–0700 IST to 8.1 g kg^{-1} at 1300–1500 IST. The water vapour mixing ratio is larger and highly variable during May: on average, it increases from 5.8 g kg^{-1} at 0600 IST to $\approx 11.2 \text{ g kg}^{-1}$ at 1300–1400 IST. The monthly mean water vapour mixing ratio is 6.7 ± 3.0 , 6.6 ± 2.5 , and $9.2 \pm 5.0 \text{ g kg}^{-1}$ during March, April and May, respectively. The day-to-day variation of mixing ratio is the largest in May (when the average water vapour content is quite high) and the least in March.

From the diurnal variations of wind, temperature, and humidity observed during the spring season we can speculate the following. The variations in all the above stated meteorological variables are more prominent in March, when the background mean flow is weak. The large-scale circulation during this season is predominantly north-westerly. Orientation of the local orography suggests that the upslope winds, generated by surface heating during daytime, would be predominantly south-westerly/westerly. During the daytime, this wind is superimposed on the background north-westerly winds, which enhances the wind speed and the westerly component. Strength of this upslope flow increases during daytime and may have contributed to increases in wind speed observed during the afternoon. This may be the reason for the larger spread in wind direction, with significant westerly winds, observed during the afternoon (Fig. 6). These winds advect air from humid forested areas to the west/south-west, especially during daytime, which increase the surface-layer specific humidity until afternoon, encouraging the formation of boundary-layer clouds in the afternoon over the region. In contrast, during nighttime, the downslope flow is largely easterly/north-easterly. The background wind being north-westerly, this downslope easterly wind reduces the net flow and reduces the westerly component in the background north-westerly winds, as observed during the nighttime. The flow is then predominantly north-westerly during nighttime, as observed, with advected air from relatively barren hills (compared to airflow from forested areas in the west/south-west during daytime). This, together with the reduction in evapotranspiration during night, reduces the mixing ratio and RH , as observed during nighttime, especially during the post-midnight period.

However, as the site is located near the ridge and that the prevailing background north-westerly winds are rather strong, a complete reversal associated with the katabatic and anabatic flows are not observed, though the effect of these mountain circulations are discernible, especially in the consistent change in wind direction (albeit with small magnitude) and wind speed. The dissipation of ABL clouds after sunset also supports this inference. The relatively warm nights with nearly constant (or increasing) temperature during the pre-midnight period may have resulted from the vertical mixing of surface-layer air due to wind-shear generated turbulence, which prevents the stabilization of cold air near the surface (e.g., Gustavsson et al. 1998).

4.3 Variations of Normalized Standard Deviations

Standard deviations of the wind-velocity components normalized by friction velocity (e.g., σ_w/u_*) can be used to verify the applicability of Monin–Obukhov similarity theory (MOST) for the observations and existence of equilibrium conditions in the ABL (Foken and Wichura 1996; Geissbuhler et al. 2000). The variations of σ_w/u_* and standard deviations of tem-

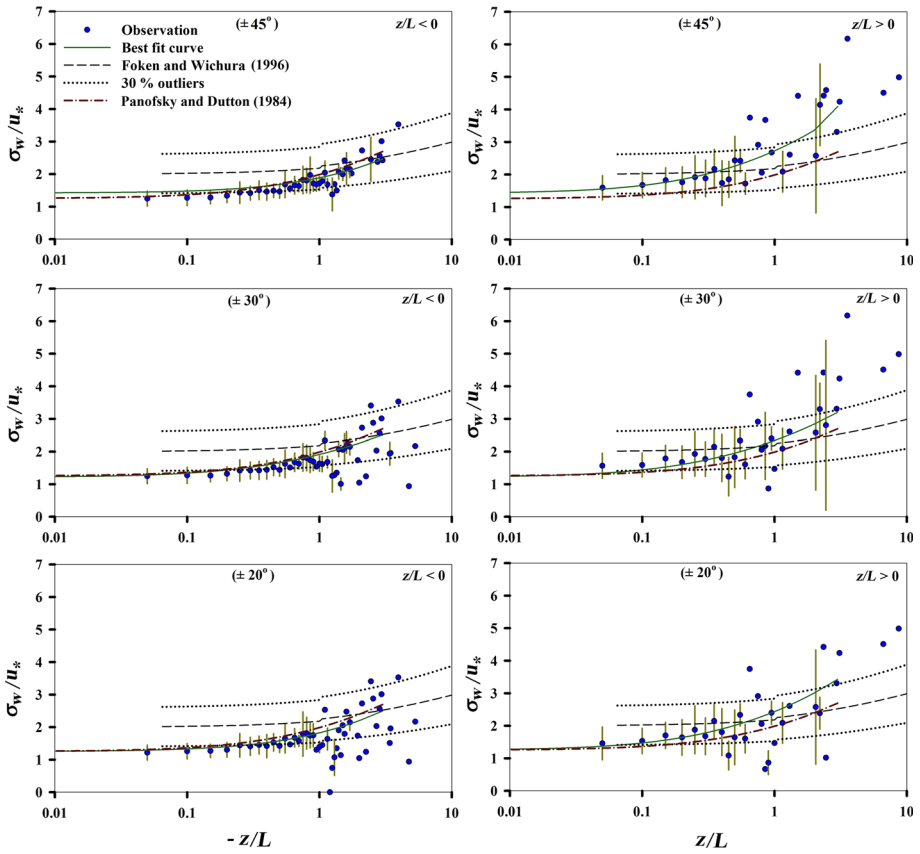


Fig. 7 Variations of bin-averaged σ_w/u_* with z/L for unstable ($z/L < 0$) and stable ($z/L > 0$) conditions for different angles of attack (within $\pm 20^\circ$, $\pm 30^\circ$, and for all ranges within $\pm 45^\circ$) at 27-m height. *Solid line* represents the curve fitted using the present observations. *Dashed line* represents the variation derived by Foken and Wichura (1996) (FW96). *Dotted line* represents the values 30% lower or larger than FW96. The variation proposed by Panofsky and Dutton (1984) is shown by the dashed-dotted line

perature normalized with the scaling temperature (i.e., σ_θ/T_*), also referred to as integral turbulence characteristics, are also used to assess the quality of data and turbulence parameters derived over complex terrain (Foken and Wichura 1996). While the above normalized standard deviations remain constant in neutral conditions, they are expected to undergo a power-law type variation as a function of z/L in the unstable surface layer, when the stress is non-zero (e.g., Stull 1988; Moraes et al. 2005; Martins et al. 2009; Trini Castelli et al. 2014).

Figure 7 shows the variations of bin-averaged σ_w/u_* with z/L for unstable ($z/L < 0$) and stable ($z/L > 0$) conditions for different angles of attack (within $\pm 20^\circ$, $\pm 30^\circ$, and for all ranges within $\pm 45^\circ$) at the 27-m level. Results for different angles of attack are presented here to investigate any inconsistency in the observations as a function of angle of attack (though the observations made using USA-1 sonic anemometers equipped with a three dimensional head-correction are corrected for angle of attack within the range of $\pm 45^\circ$). The dashed curve represents the variations derived by Foken and Wichura (1996) (FW96), while the dotted curve represents the values 30% lower or larger than FW96. The corresponding variation proposed by Panofsky and Dutton (1984) is shown by the dashed-dotted curve. The

solid curve represents the curve fitted using the following relation (Foken and Wichura 1996; Moraes et al. 2005)

$$\frac{\sigma_w}{u_*} = A \left[1 + B \left(\frac{z}{L} \right) \right]^C. \quad (4)$$

The values of A , B and C obtained from the present study for unstable conditions are 1.2, 7.5, and 0.3, respectively (for all observations). The variations of σ_w/u_* with z/L for unstable conditions for different angle of attack are almost consistent with each other (except for improved statistics obtained with a wider range of angle of attack) and are mostly within $\pm 30\%$ of FW96 for $-3 < z/L < 0$. It has been suggested that the data may be considered as of good quality if the difference between the measured integral characteristics and those calculated using empirical model is less than about 30%. On the contrary, if additional mechanical turbulence caused by other sources (e.g., obstacles) or artefacts due to terrain effects, surface inhomogeneity, or the measuring device itself are present, the measured value of the integral characteristics of the scalars would be substantially larger than those proposed (e.g., Panofsky and Dutton 1984; Foken and Wichura 1996). The empirical model of Panofsky and Dutton (1984) has $A = 1.25$, $B = 3.2$ and $C = 1/3$, and the curve shows general agreement with the present observation for $-3 < z/L < 0$. During neutral conditions ($z/L \approx 0$), the value of σ_w/u_* is found to be ≈ 1.2 , which is comparable to the value reported by Moraes et al. (2005) and Panofsky and Dutton (1984).

Figure 8 shows the variation of σ_θ/T_* with z/L for different ranges of the angle of attack. Under unstable conditions, variation of σ_θ/T_* with z/L shows a relationship (fitted line in Fig. 8):

$$\frac{\sigma_\theta}{T_*} = 2.13 \left(\frac{z}{L} \right)^{-1/3}. \quad (5)$$

This relationship and coefficients are in agreement with the general understanding that the variation of σ_θ/T_* with z/L follows a power-law variation with an index of $-1/3$ during unstable conditions (Wyngaard et al. 1971; Stull 1988; Moraes et al. 2005).

Notwithstanding the complexity of the terrain and the corrections applied to the measurements, comparison of Figs. 7 and 8 with the empirical model relationships reported in the literature shows that the present data quality is sufficient for estimating turbulent fluxes. However, it may also be noted here that consideration of the integral statistics alone may not be adequate to provide complete quality assessment.

Unlike vertical winds, the variations of normalized standard deviations of u and v with z/L may not follow MOST, as they might be significantly influenced by large-scale convective cells having a length scale comparable with the mixed-layer height, z_i (e.g., Moraes et al. 2005). These variables are to be scaled by the convective velocity scale (w_*) and are related to z_i/L rather than z/L . As the present observations do not have direct information on z_i , variations of the normalized standard deviations of u and v as a function of z_i/L are not presented here.

4.4 Diurnal Variations of e , H , τ and z/L

Monthly mean diurnal variations of e , H , τ and z/L derived from the tower-based fast-response sonic anemometer measurements at the 27-m level during March, April, and May are shown in Fig. 9. The diurnal variation of H is prominent; it increases systematically after 0800 IST, attains peak values during 1200–1400 IST and decreases to negative nighttime values by 1800 IST. The time of occurrence of the peak H values is in agreement with the

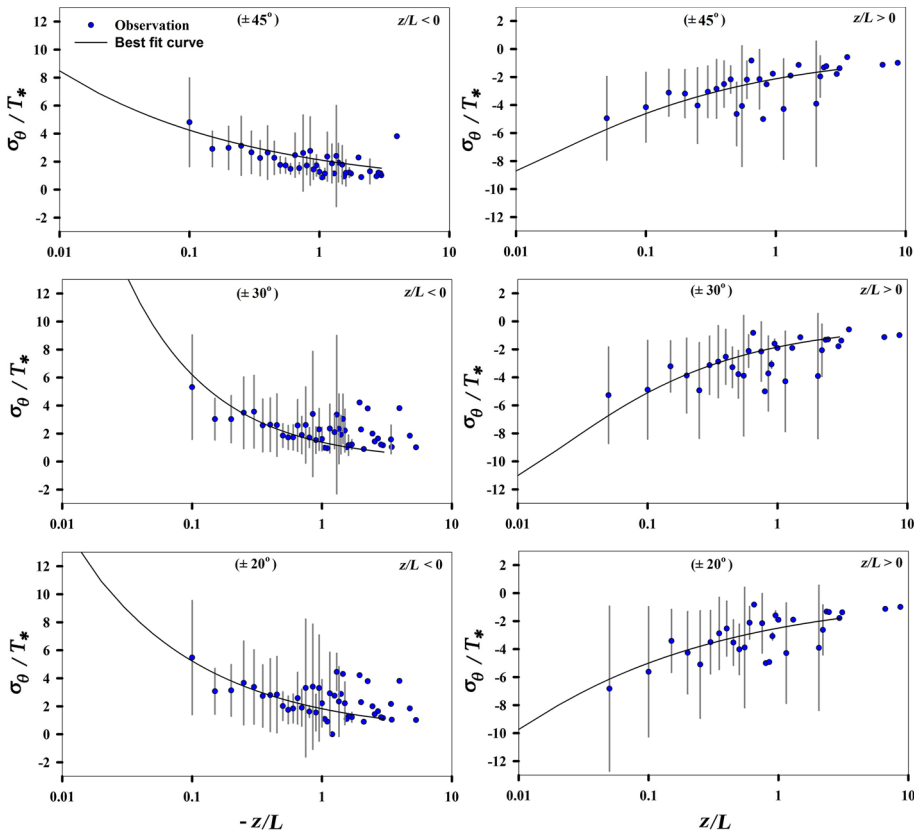


Fig. 8 Similar to Fig. 9, but for of σ_θ / T_* with z/L . Solid line represents the curve fitted using the present observations

phase of the largest surface heating due to the incoming shortwave solar flux (Fig. 3). The peak value of H is the largest ($353 \pm 147 \text{ W m}^{-2}$) in May and the least ($222 \pm 46 \text{ W m}^{-2}$) in March. The peak value of H during April–May is larger than the corresponding values observed at some tropical regions. Such high values of H over this Himalayan station during spring are aided by the large values of shortwave radiative flux and the vertical circulations that might prevail during the daytime. A rather weak downward transport of heat is observed during the nighttime (typically H in the range of -10 to -25 W m^{-2}), and that is more prominent during April–May. In contrast, the magnitude of the nighttime H is least during March (typically $+5$ to -10 W m^{-2}). The net diurnal mean H is from surface to atmosphere during the spring season and 50 W m^{-2} .

The diurnal variation of e during March is quite small, while values of e show an enhancement in the afternoon (especially during 1500–1600 IST) during April and May. These afternoon peak values of e observed during April and May are almost 30–50% larger than the corresponding values observed at night, indicating the magnitude of the increase in the turbulence intensity during the afternoon. Note that, during April and May, the peak values of e are attained about 2h after the peak values of the incoming shortwave flux and H . However, as seen earlier, the turbulence generated by wind shear increases in the afternoon period, until late evening or early night. The observed

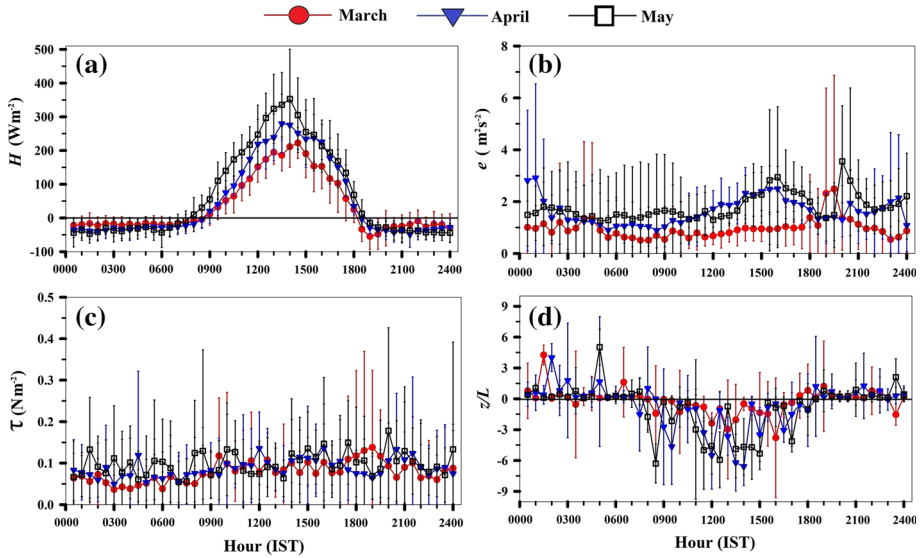


Fig. 9 Monthly mean diurnal variations of **a** sensible heat flux (H), **b** turbulent kinetic energy (e), **c** momentum flux (τ) and **d** stability parameter (z/L) during March, April, and May of 2013. Vertical bars represent the standard deviations

variations in e clearly show the continued increase in the production of turbulence by the systematic increase in wind shear during the afternoon period, even after the intensity of the thermals decreases during the afternoon. Interestingly, the nocturnal values of e also increase from March to May, which might be due to the corresponding increase in wind shear, and thus an increase in turbulence intensity. The stress τ observed during the March–May period does not show any discernible diurnal variation, although the values during the afternoon are marginally larger than those during the post-midnight period.

The diurnal variation of z/L (Fig. 9d) shows the development of instability during the daytime while the nocturnal surface layer is generally stable or neutral. Analysis shows that during the daytime unstable conditions prevail for 85 % of the time, while the frequency of occurrence of stable conditions is 14 % at the 27-m level. In contrast 10 % of the nighttime is either unstable or neutral, and stable conditions prevail only for about 90 % of the time at the 27-m level. Inferences made using the observations at the 12-m level are also similar. The significant occurrence of nighttime neutral or unstable conditions is associated with the large wind shear during the early night, which leads to mixing of surface-layer air upwards.

As the surface-layer turbulence is likely affected by wind speed, diurnal variations of H , e , τ and z/L during the days when the daily mean wind speed $< 1.5 \text{ m s}^{-1}$, moderate ($1.5\text{--}4 \text{ m s}^{-1}$) and large ($> 4 \text{ m s}^{-1}$) are further investigated. As shown in Fig. 10, the e values are distinctly larger when the mean wind speed is larger, with an average enhancement from $0.7 \text{ m}^2 \text{ s}^{-2}$ during calm conditions to about $2 \text{ m}^2 \text{ s}^{-2}$, when the winds are strong. The momentum flux almost doubles between calm and strong wind conditions. The H values show an enhancement of 50 W m^{-2} around noon during strong winds, compared to calm periods.

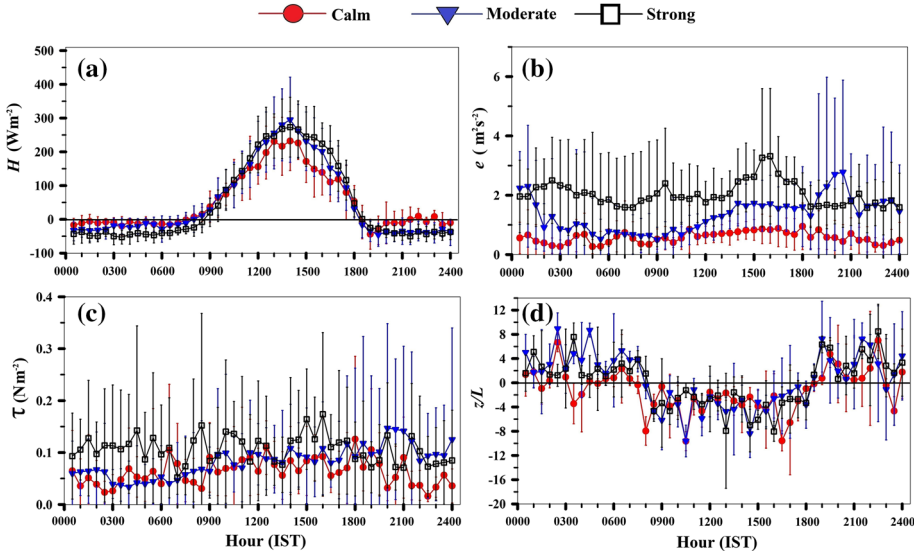


Fig. 10 Same as Fig. 9, but for different daily mean wind conditions: calm ($<1.5 \text{ m s}^{-1}$), moderate ($1.5\text{--}4 \text{ m s}^{-1}$) and strong ($>4 \text{ m s}^{-1}$)

5 Conclusions

Surface-layer characteristics over the mountainous terrain of the south-central Himalayas are largely unknown. New observations of the diurnal variations of surface-layer characteristics derived from fast-response sonic anemometer at two levels (at 12 and 27 m on a meteorological tower) near a mountain ridge at the south-central Himalayan station, Nainital (29.4° N , 79.5° E , 1926 m surface elevation) during the spring season (March–May of 2013) have been described. We have focussed on spring since significant heating of the surface, together with fair weather conditions prevail during this season, providing favourable conditions for the systematic diurnal evolution of the ABL.

Aided by the favourable solar declination, high surface elevation and clear-sky conditions, the incoming shortwave flux at the surface attains peak noontime values of $1000\text{--}1100 \text{ W m}^{-2}$ during this season. The wind speed generally increases from a minimum at 0900 IST to a maximum around the evening and early night. The wind shear is quite significant during the evening and night, with its phase similar to the wind speed; the peak wind shear increases from March (typically 0.06 s^{-1}) to April–May (typically 0.2 s^{-1}). In general, the wind direction is mostly within a cone of $285^\circ\text{--}315^\circ$ during the nighttime and forenoon, while the occurrence of westerly winds ($265^\circ\text{--}305^\circ$) increases during the afternoon. This reveals the effect of the diurnally varying upslope and downslope winds and the drainage circulation in modulating flow over the mountain ridge, which experiences a strong prevailing large-scale synoptic flow. As the site is located near the ridge and that the prevailing background north-westerly flow is rather strong, a complete reversal associated with the katabatic and anabatic winds is not observed. Dry conditions (mean $RH < 40\%$) prevail during the night and morning period (when the flow is predominantly north-westerly from the barren areas), while the RH generally increases to $>80\%$ during the daytime until about 1500–1600 IST (when the occurrence of westerly winds is frequent, advecting humid air from the forest areas). The observed diurnal variation in RH arises mainly due to the enhancement in water vapour

mixing ratio (which typically increases from 4.1 g kg^{-1} at 0700 IST to 10.5 g kg^{-1} at 1500–1600 IST) rather than the variations associated with temperature. This aids the formation of boundary-layer clouds during the afternoon period and their dissipation after sunset.

Large surface heating due to the incoming solar flux during the daytime leads to the enhancement of H , which attains peak values (at 1200–1400 IST) of $353 \pm 147 \text{ W m}^{-2}$ in May. The diurnal mean upward transfer of heat from surface to atmosphere during the spring season is 50 W m^{-2} . The peak H value occurs almost in phase with the incoming solar flux. The diurnal variation of e is significant only during April–May, when their peak values occur at 1500–1600 IST, about 2 h after the peak values of the incoming shortwave flux and H are attained. This phase delay in the diurnal variations of e indicates the continued increase in turbulence generation by the increase in wind shear during the course of the day, even after the intensity of the thermals decreases. On average, the magnitude of e is found to increase from about $0.7 \text{ m}^2 \text{ s}^{-2}$ during calm periods to more than $2 \text{ m}^2 \text{ s}^{-2}$ when the winds are strong ($>4 \text{ m s}^{-1}$) corresponding to the enhancement in the peak noontime values of $H \approx 50 \text{ W m}^{-2}$ from calm conditions to strong winds.

Variations of the standard deviations of vertical velocity normalized by friction velocity (σ_w/u_*) and temperature normalized with scaling temperature (σ_θ/T_*) as a function of stability (z/L) indicate a power-law variation during unstable conditions, with an index of $1/3$ for the former and $-1/3$ for the latter. The coefficients defining the above variations are found to be in agreement with those derived over both flat and complex terrain. The value of σ_w/u_* for neutral conditions ≈ 1.2 .

This study provides further support that the statistics and parametrization of turbulence characteristics in the surface layer over complex terrain are similar to those over flat homogeneous terrain, at least for the limited conditions (primarily moderate–strong winds) observed here.

Acknowledgments This work has been carried out as part of IGBP-NOBLE Project. We thank the Director, ARIES Nainital; Director, SPL, Thiruvananthapuram and Project Director, ISRO-IGBP for their valuable support. Raman Solanki is thankful to the Indian Space Research Organization for sponsoring the PhD Research Fellowship. The authors thank the anonymous reviewers for their valuable suggestions.

References

- Arya SP (2001) Introduction to micro-meteorology, 2nd edn. Academic, San Diego, 420 pp
- Aubinet M, Vesala T, Papale D (eds) (2012) Eddy covariance: a practical guide to measurement and data analysis. Springer, Dordrecht, 438 pp
- Barr S, Orgill MM (1989) Influence of external meteorology on nocturnal valley drainage winds. *J Appl Meteorol* 28:497–517
- Bianco L, Djalalova IV, King CW, Wilczak JM (2011) Diurnal evolution and annual variability of boundary-layer height and its correlation with other meteorological variables in California's Central Valley. *Boundary-Layer Meteorol* 140:491–511. doi:10.1007/s10546-011-9622-4
- Chen X, Anel JA, Su Z, de la Torre L, Kelder H, van Peet J, Ma Y (2013) The deep atmospheric boundary layer and its significance to the stratosphere and troposphere exchange over the Tibetan plateau. *PLoS ONE* 8(2):e56909. doi:10.1371/journal.pone.0056909
- Foken T, Wichura B (1996) Tools for quality assessment of surface-based flux measurements. *Agric For Meteorol* 78:83–105
- Geissbuhler P, Siegwolf R, Eugster W (2000) Eddy covariance measurements on mountain slopes: the advantage of surface-normal sensor orientation over a vertical set-up. *Boundary-Layer Meteorol* 96:371–392
- Gustavsson T, Karlsson M, Bogren J, Sindqvist S (1998) Development of temperature patterns during clear nights. *J Appl Meteorol* 37:559–571
- Helgason W, Pomeroy JW (2012) Characteristics of the near-surface boundary layer within a mountain valley during winter. *J Appl Meteorol Climatol* 51:583–597. doi:10.1175/JAMC-D-11-058.1

- Hughes M, Hall A, Fovell RG (2007) Dynamical controls on the diurnal cycle of temperature in complex topography. *Clim Dyn* 29(2–3):277–292. doi:[10.1007/s00382-007-0239-8](https://doi.org/10.1007/s00382-007-0239-8)
- Kaimal JC, Finnigan JJ (1994) Atmospheric boundary layer flows: their structure and measurement. Oxford University Press, New York, 289 pp
- Katurji M, Sturman A, Zawar-Reza P (2011) An investigation into ridge-top turbulence characteristics during neutral and weakly stable conditions: velocity spectra and isotropy. *Boundary-Layer Meteorol* 139:143–160
- Kleissl J, Honrath RE, Dziobak MP, Tanner D, Val Martin M, Owen RC, Helmig D (2007) Understanding of upslope flows at the Pico mountaintop observatory: a case study of orographic flows on a small, volcanic island. *J Geophys Res* 112:D10S35
- Li JG, Atkinson BW (1999) Transition regimes in valley airflows. *Boundary-Layer Meteorol* 91:385–411
- Mahrt V (2006) Variation of surface air temperature in complex terrain. *J Appl Meteorol Climatol* 45:1481–1493
- Mahrt L, Heald R (1983) Nocturnal surface temperature distribution as remotely sensed from low-flying aircraft. *Agric Meteorol* 28:99–107
- Mahrt L, Vickers D, Nakamura R, Sun J, Burns S, Lenschow D, Soler M (2001) Shallow drainage and gully flows. *Boundary-Layer Meteorol* 101:243–260
- Martins CA, Moraes OLL, Acevedo OC, Degrazia GA (2009) Turbulence intensity parameters over a very complex terrain. *Boundary-Layer Meteorol* 133:35–45
- Meenu S, Rajeev K, Parameswaran K, Raju CS (2007) Characteristics of double ITCZ over the tropical Indian Ocean. *J Geophys Res* 112:D11106. doi:[10.1029/2006JD007950](https://doi.org/10.1029/2006JD007950)
- Meenu S, Rajeev K, Parameswaran K, Nair AKM (2010) Regional distribution of deep clouds and cloud top altitudes over the Indian subcontinent and the surrounding oceans. *J Geophys Res* 115:D05205. doi:[10.1029/2009JD011802](https://doi.org/10.1029/2009JD011802)
- Moraes OLL, Acevedo OC, Degrazia GA, Anfossi D, da Silva R, Anabor V (2005) Surface layer turbulence parameters over a complex terrain. *Atmos Environ* 39:3103–3112
- Nadeau DF, Pardyjak ER, Higgins CW, Huwald H, Parlange MB (2013) Flow during the evening transition over steep alpine slopes. *Q J R Meteorol Soc* 139(672):607–624
- Panday AK, Prinn RG (2009) Diurnal cycle of air pollution in the Kathmandu Valley, Nepal: observations. *J Geophys Res* 114:D09305. doi:[10.1029/2008JD009777](https://doi.org/10.1029/2008JD009777)
- Panofsky HA, Dutton JA (1984) Atmospheric turbulence. Wiley, New York, 397 pp
- Pant P, Hegde P, Dumka UC, Saha A, Srivastava MK, Sagar R (2006) Aerosol characteristics at a high latitude location during ISRO-GBP land campaign-II. *Curr Sci* 91:1053–1061
- Papadopoulos KH, Helmis CG (1999) Evening and morning transition of katabatic flows. *Boundary-Layer Meteorol* 92:195–227
- Ramanathan V, Ramana MV (2005) Persistent, widespread, and strongly absorbing haze over the Himalayan foothills and the Indo-Gangetic plains. *Pure Appl Geophys* 162:1609–1626
- Richiardone R, Giampiccolo E, Ferrarese S, Manfrin M (2008) Detection of flow distortions and systematic errors in sonic anemometry using the planar fit method. *Boundary-Layer Meteorol* 128:277–302
- Rotach MW, Zardi D (2007) On the boundary-layer structure over highly complex terrain: key findings from MAP. *Q J R Meteorol Soc* 133:937–948. doi:[10.1002/qj.71](https://doi.org/10.1002/qj.71)
- Solanki R, Singh N, Pant P, Dumka UC, Bhavani Kumar Y, Srivastava AK, Bist S, Chandola HC (2013) Detection of long range transport of aerosols with elevated layers over high altitude station in the central Himalayas: A case study on 22 and 24 March 2012 at ARIES, Nainital. *Indian J Radio Space Phys* 42:332–339
- Sun F, Ma Y, Li M, Ma W, Tian H, Metzger S (2007) Boundary layer effects above a Himalayan valley near Mount Everest. *Geophys Res Lett* 34:L08808. doi:[10.1029/2007GL029484](https://doi.org/10.1029/2007GL029484)
- Stewart JQ, Whiteman CD, Steenburgh WJ, Bian X (2002) A climatological study of thermally driven wind systems of the U.S. intermountain West. *Bull Am Meteorol Soc* 83:699–708
- Stull RB (1988) An introduction to boundary layer meteorology. Kluwer Academic Publishers, Dordrecht, 670 pp
- Trini Castelli S, Falabino S, Mortarini L, Ferrero E, Richiardone R, Anfossi D (2014) Experimental investigation of the surface layer parameters in low wind conditions in a suburban area. *Q J R Meteorol Soc* 140:2023–2036
- Vickers D, Mahrt L (2006b) A solution for flux contamination by mesoscale motions with very weak turbulence. *Boundary-Layer Meteorol* 118:431–447
- Whiteman CD (1990) Chapter 2: observations of thermally developed wind systems in mountainous terrain. In: Blumen W (ed) Atmospheric processes over complex terrain. Meteorological monographs, vol 23(45). American Meteorological Society, Boston, pp 5–42

- Whiteman CD (2000) *Mountain meteorology fundamentals and applications*. Oxford University Press, New York, 355 pp
- Wilczak JM, Oncley SP, Stage SA (2001) Sonic anemometer tilt correction algorithms. *Boundary-Layer Meteorol* 99:127–150
- Wyngaard JC, Cote' OR, Izumi Y (1971) Local free convection, similarity, and the budgets of shear stress and heat flux. *J Atmos Sci* 28:1171–1182
- Yuan R, Kang M, Park S, Hong J, Lee D, Kim J (2007) The effect of coordinate rotation on the eddy covariance flux estimation in a hilly Koflux forest site. *Korean J Agric For Meteorol* 9:100–108
- Yuan R, Kang M, Park SB, Hong J, Lee D, Kim J (2011) Expansion of the planar-fit method to estimate flux over complex terrain. *Meteorol Atmos Phys* 110:123–133. doi:[10.1007/s00703-010-0113-9](https://doi.org/10.1007/s00703-010-0113-9)